

Resting state fMRI-based temporal coherence mapping

Abbreviated title: temporal coherence mapping

Ze Wang, PhD

ORCID: 0000-0002-8339-5567

Department of Diagnostic Radiology and Nuclear Medicine

University of Maryland School of Medicine

670 W. Baltimore St, Baltimore, MD 20201

ze.wang@som.umaryland.edu

Conflict of interest: none

Data availability statement: the HCP data is freely available from the HCP consortium.

Ethics approval statement: data reanalysis has been approved by IRB. Patient consent forms were obtained by HCP.

Acknowledgements

The research effort involved in this study was supported by NIH/NIA grants: R01AG060054, R01 AG070227, AG060054-02S1, and by the support of the University of Maryland, Baltimore, Institute for Clinical & Translational Research (ICTR) and the National Center for Advancing Translational Sciences (NCATS) Clinical Translational Science Award (CTSA) grant number 1UL1TR003098. Both imaging and behavior data were provided by the Human Connectome

Project, WU-Minn Consortium (Principal Investigators: David Van Essen and Kamil Ugurbil; 1U54MH091657) funded by the 16 NIH Institutes and Centers that support the NIH Blueprint for Neuroscience Research; and by the McDonnell Center for Systems Neuroscience at Washington University in St. Louis. The author thank the Human Connectome Project for open access to its data, thank Donghui Song, Qiu Ge, Yiran Li for data organization, transferring, and processing assistance.

Abstract

Long-range temporal coherence (LRTC) is quite common to dynamic systems and is fundamental to the system function. LRTC in the brain has been shown to be important to cognition. Assessing LRTC may provide critical information for understanding the potential underpinnings of brain organization, function, and cognition. To facilitate this overarching goal, we provide a method, which is named temporal coherence mapping (TCM), to explicitly quantify LRTC using resting state fMRI. TCM is based on correlation analysis of the transit states of the phase space reconstructed by temporal embedding. A few TCM properties were collected to measure LRTC, including the averaged correlation, anti-correlation, the ratio of correlation and anticorrelation, the mean coherent and incoherent duration, and the ratio between the coherent and incoherent time. TCM was first evaluated with simulations and then with the large Human Connectome Project data. Evaluation results showed that TCM metrics can successfully differentiate signals with different temporal coherence regardless of the parameters used to reconstruct the phase space. In human brain, TCM metrics except the ratio of the coherent/incoherent time showed high test-retest reproducibility; TCM metrics are related to age, sex, and total cognitive scores. In summary, TCM provides a first-of-its-kind tool to assess LRTC and the imbalance between coherence and incoherence; TCM properties are physiologically and cognitively meaningful.

Keywords: long-range temporal coherence, cognition, resting state fMRI, temporal embedding

Introduction

The human brain is a self-organized system (Willshaw 2006, Singer 2009, Haken 2012) which relies on the time varying activity to coordinate and adapt its functions. Understanding the temporal dynamics of brain activity is crucial to understanding the individual differences of brain function and the neuropsychopathologies associated with neuropsychiatric conditions. A critical aspect of these temporal dynamics is the emergence of long-range temporal coherence or correlation (LRTC), meaning that brain activity at one moment can influence future activities. LRTCs have been well observed at different time scales using neuronal spike recordings, electrophysiological data, hemodynamic response as measured by functional MRI (Suckling, Wink et al. 2008, Wink, Bullmore et al. 2008, He, Zempel et al. 2010, He 2011). They have been shown to be crucial to high-order brain functions including decision making, memory, learning, network reorganization (Botcharova, Farmer et al. 2014), attention, perception, coordination, etc (Pesaran, Pezaris et al. 2002, Buzsáki and Draguhn 2004, Womelsdorf, Fries et al. 2006, Womelsdorf, Fries et al. 2006, Buschman and Miller 2007, Saleh, Reimer et al. 2010, Dean, Hagan et al. 2012, Thut, Miniussi et al. 2012, Palva, Zhigalov et al. 2013, Wong, Fabiszak et al. 2016, Shewcraft, Dean et al. 2020). LRTC of a single brain region may initiate or influence cross-regional effective connectivity and communications (Fries 2005, Teki, Chait et al. 2013, Fries 2015, Lu, Xu et al. 2017, Pesaran, Vinck et al. 2018).

Given the importance of LRTC in functional brain organization and neurocognition, several methods have been used to quantify it. The most intuitive one is the auto-correlation function (ACF) since a slowly decaying ACF indicates LRTC. In the case where ACF is not reliable to estimate, LRTC can be assessed with the Hurst exponent (Hurst 1951) or its surrogates such as the exponent of the apparent power law function fitted from the logarithm of the spectrum or the linear line slope estimated by the detrended fluctuation analysis (DFA) (Peng, Havlin et al. 1995). While these methods have been proven to be useful for evaluating LRTCs, none of them directly

considers the transit states of the underlying dynamic process. According to theoretical work and neuroscience experiments, the human brain nearly operates at a self-organized criticality, from where the LRTCs emerge (Rubinov, Sporns et al. 2011, Deco and Jirsa 2012). At the critical condition, the dynamic system frequently switches between different intermediate state around the attracting point (Beggs and Plenz 2003, Friedman, Ito et al. 2012, Munoz 2018) and LRTCs emerge from the inter-state correlations across a long time range and can be accordingly directly characterized through the inter-transit state correlations. During the course, we can separate correlated states from anti-correlated transit states, so that we can directly evaluate the macroscopic level brain temporal coherence and anti-coherence (C/A) balance. Considering the fact of that at the microscopic level, it is well known that neurons preserves a neuronal excitation and inhibition (E/I) balance that is important to neuron function (Okun and Lampl 2008), the macroscopic level C/A balance may carry important information about brain self-regulation and brain function.

We have previously studied temporal coherence of resting state fMRI using the temporal embedding-based approximate entropy calculation (Wang, Li et al. 2014). The approximate entropy, the so-called Sample Entropy (SampEn) (Richman and Moorman 2000) is calculated by the negative logarithm of the probability of that two similar phase space transit states (Nolte 2010) will remain similar if the dimension of reconstructed phase space increased by one, meaning that the length of the embedding vector increases by one. While the SampEn-based entropy mapping has been shown to be informative of brain health and neurocognitions (Zhou, Zhuang et al. 2016, Da Chang 2018, Donghui Song 2019, Xue, Yu et al. 2019, Liu, Song et al. 2020, Wang 2020, Wang and Initiative 2020), it only provides an indirect way to assess temporal coherence. Moreover, it does not consider temporal anti-coherence, not to mention the C/A balance. To bridge this gap, we proposed a new method: temporal coherence mapping (TCM), to directly quantify LRTC of a dynamic system through the correlations between all intermediate states of

the phase space of a dynamic system (Nolte 2010). Phase space is mathematically defined as a collection of all states of a system. It is widely used to study the behavior of the time evolution trajectory of the system status and to use current state to predict future behavior. According to Takens' theorem (Takens 1981), the phase space can be reliably reconstructed from the measure one-dimensional timeseries through temporal embedding. Each embedding vector identified during phase space reconstruction was considered representing an intermediate state. The inter-state correlation was then calculated and averaged across all possible pairs of embedding vectors. By aggregating the positive and negative correlations separately, we also provided a way to examine the temporal C/A ratio. Temporal embedding has been used in our previous brain entropy mapping work, but the length of the vectors is often 2 or 3. By contrast, we used much longer embedding vectors in TCM so that inter-vector correlations can be reliably estimated. Temporal coherence was then measured as the mean positive correlation coefficient of those embedding vectors and temporal ant coherence was by the mean negative correlation coefficient. Their ratio was used to assess the C/A balance. Another C/A balance measure was defined by the ratio between the average length of the diagonal line segments of the positive correlation coefficient matrix and that of the diagonal line segments of the negative correlation coefficient matrix. The diagonal lines in the correlation coefficient matrix of the embedding vectors indicate how long the dynamic system stays in certain transit states and are useful for indicating periodic behavior of the system (Marwan, Romano et al. 2007). We applied TCM to brain activity measured with resting state functional MRI (rsfMRI) and empirically examined the temporal brain C/A balance based on these TCM C/A metrics at the macroscopic level for the first time. Our hypothesis was that resting healthy brain presents spatially distributed LRTCs with higher LRTCs in grey matter than in white matter; the long-range positive correlations and long-range negative correlations are well balanced in the brain as reflected by a C/A ratio <1 across the brain. We also hypothesized that LRTCs present regional correlations to physiological measures and neurobehavior measures.

Materials and Methods

Ethics statement

Data acquisition and sharing have been approved by the HCP parent IRB. Written informed consent forms have been obtained from all subjects before any experiments. This study re-analyzed the HCP data and data Use Terms have been signed and approved by the WU-Minn HCP Consortium.

Data included

rsfMRI data, demographic data, and neurobehavior data from 862 healthy young subjects (age 22-37 yrs, male/female=398/464) were downloaded from HCP. The range of education years was 11-17 yrs with a mean and standard deviation of 14.86 ± 1.82 yrs. The rsfMRI data used in this paper were the extended processed version released on July 21 2017. Each subject had four rsfMRI scans acquired with the same multi-band sequence (Moeller, Yacoub et al. 2010) but the readout directions differed: readout was from left to right (LR) for the 1st and 3rd scans and right to left (RL) for the other two scans. The purpose of acquiring different scans with opposite phase encoding directions was to compensate the long scan time induced image distortion. MR scanners all present field strength (B0) inhomogeneity, which causes signal distortion because of the imperfect excitation using the radiofrequency pulses that are tuned to the frequency determined by the ideal B0. While the B0 inhomogeneity caused distortions can be well corrected using two additionally acquired calibration scans using the opposite phase encoding directions: one is with LR and the other is with RL, HCP acquired two LR and two RL rsfMRI scans for the purpose of assessing the potential residual effects after the distortion correction and to assess the test-retest stability of rsfMRI measure. Each scan had 1200 timepoints. Other acquisition

parameters for rsfMRI were: repetition time (TR)=720 ms, echo time (TE)=33.1ms, resolution 2x2x2 mm³. The pre-processed rsfMRI data in the Montreal Neurological Institute (MNI) brain atlas space were downloaded from HCP and were smoothed with a Gaussian filter with full-width-at-half-maximum = 6mm to suppress the residual inter-subject brain structural difference after brain normalization and artifacts in rsfMRI data introduced by brain normalization.

Temporal coherence mapping (TCM)

Phase space reconstruction through temporal embedding is illustrated in the top panel in Fig. 1. Denote a time series, for example, the time series of a brain voxel, by $x = [x_1, x_2, \dots, x_N]$, where N is the number of time points. The phase space of the underlying dynamic system can be reconstructed by a series of embedding vectors, each with m consecutive points extracted from x : $u_i = [x_i, x_{i+1}, \dots, x_{i+m-1}]$, where $i = 1$ to $N-m+1$, m is the pre-defined embedding vector length. As illustrated by the lower panel of Fig. 1, for a specific time series x , TCM is to calculate the correlation coefficient matrix of the embedding vectors. For the simplicity of description, this matrix was named the TCM matrix in the following text.

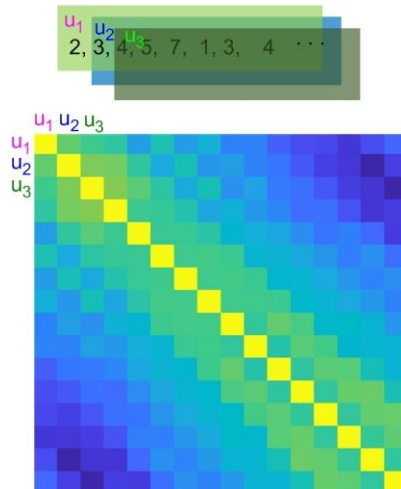


Figure 1. Illustration of TCM. The upper panel shows the moving window-based embedding vector extractions; the lower panel shows the TCM matrix (the correlation coefficient matrix) of those embedding vectors. Yellow means a correlation coefficient of 1; blue means negative correlations. u_1, u_2, u_3 denote three embedding vectors.

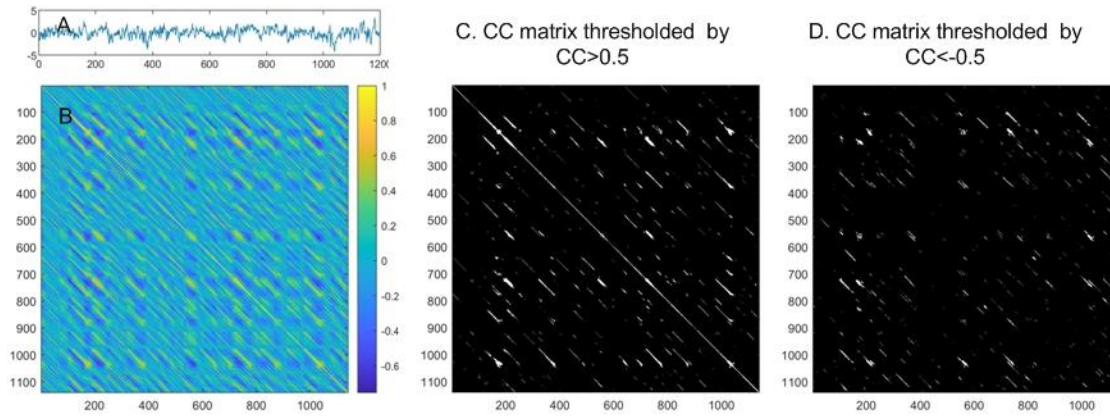


Fig. 2. The TCM matrix of the embedding vectors of a rsfMRI time series extracted from a representative HCP rsfMRI scan in the precuneus. A) The rsfMRI time series, B) The non-thresholded correlation coefficient matrix, C and D are the binarized TCM matrix thresholded by $CC > 0.5$ and $CC < -0.5$, respectively.

While the TCM matrix provides a way to observe the temporal coherence patterns such as the positive and negative correlation, the decaying and potentially recurring correlation from the main diagonal to the off-center diagonals, the balance between the positive and negative correlations etc, we need some metrics to quantify these properties. Below, we provided several potentially valuable property metrics for condensing the information provided by the TCM matrix.

- (1) The first two are the temporal coherence (TC) and the temporal anti-coherence (TAC) which are calculated as the mean positive correlation coefficient and the mean negative correlation coefficient:

$$TC = \frac{\sum_i^M cc_i}{\sum_i^M H(cc_i)} \quad \text{for all } cc_i > 0$$

$$TAC = \frac{\sum_i^M -cc_i}{\sum_i^M H(-cc_i)} \quad \text{for all } cc_i < 0$$

where $M=(N-m+1)*(N-m)$ is the total number of off-diagonal elements of the correlation coefficient matrix. $H(.)$ is the Heaviside function:

$$H(x) = \begin{cases} 1, & x > 0 \\ 0, & x \leq 0 \end{cases}$$

(2) The third is the *C/A balance measure 1 (CAR1)*: TC/TAC .

(3) The last three measures are based on the mean length of the continuous diagonal line segments of the binarized TCM matrix. The mean length of the continuous diagonal lines is defined in the recurrent plot analysis for measuring the divergency behavior of the dynamic system (Marwan, Romano et al. 2007). In this paper, we calculate this length for the positive TCM matrix and negative TCM matrix separately. As shown in Fig. 2, the TCM matrix can be binarized with a threshold to only retain the positions with stronger than the correlation strength cutoff. Isolated dots in the binarized matrix indicate rare transit states. In other words, they do not persist in time, or they simply fluctuate too much. By contrast, the continuous diagonal line segments suggest that the system revisits the transit state represented by the embedding vectors at the corresponding coordinates of these segments many times. The length of those diagonal line segments provides an estimate of how long these transit states stick together. By hard-thresholding the TCM matrix with a positive threshold r , we can get a binarized positive correlation coefficient matrix (1 means $CC > r$, 0 means $CC \leq r$). A negative threshold $-r$ can be used to get a binarized negative TCM matrix (1 means $CC < -r$, 0 means $CC \geq -r$). The following two measures can be used to measure the recurrence of coherent (positively correlated) and incoherent

(negatively correlated) transit states, separately. Their ratio can be taken as another C/A balance indicator.

MLP: the mean length of the diagonal line segments of the binarized positive TCM matrix.

MLN: the mean length of the diagonal line segments of the binarized negative TCM matrix.

MLP/MLN

Algorithm 1. TCM

input:

x - time series with N timepoints
w - embedding vector length
r - correlation coefficient threshold
g - gap between adjacent embedding vectors

output:

TC - mean positive correlation coefficient
TAC - mean negative correlation coefficient
CAR1 - TC/TAC
MLP - mean length of the diagonal lines of
positive TCM matrix
MLN - mean length of the diagonal lines of
negative TCM matrix
CAR2 - MLP/MLN

```
1  DIA_S=w/3
2  DIA_E=w
3  Nv=int((N-w+1)/g) //number of embedding vectors
4  max_dia=(Nv-DIA_E)*g
5  M=N-w-1
6  Totnum_cc = Nv*(Nv-1)/2-DIA_E*(DIA_E+1)/2
7  TC=TAC=0
8  MLP=MLN=0
9  num_plen=num_nlen=0
10 for (l=DIA_S*g; l<max_dia; l+=gap)
11     tlen_end=tlen-w-l
12     reset flags for detecting a diagonal line
13     seg_new=0; seg_s=0; seg_e=0;
14     for(i=0; i < tlen_end; i=i+gap)
15         find embedding vectors from x at position i and i+l*gap
16         calculate their correlation cc
17         if(cc>0) add cc to TC
18         else    add cc to TAC
19         if(cc>r)
```

```

20     if(seg_new==0) // find a new diagonal line
21         // record the start point and set the flag
22         seg_s=i; seg_e=i+1; seg_new=1;
23     else // cotinuation of an existing line
24         seg_e+1 -> seg_e
25     else
26         // set the end of the line if needed
27         if(seg_new==1)
28             seg_new=0; pseglen=seg_e-seg_s;
29             // exclude the isolated point
30             if(pseglen>1)
31                 num_plen+1->num_plen; MLP = MLP+pseglen;
32     if(cc<-thr)
33         if(nseg_new==0) // find a new diagonal line
34             nseg_s=i; nseg_e=i+1; nseg_new=1;
35         else
36             nseg_e+1 -> nseg_e;
37     else
38         if(nseg_new==1)
39             nseg_new=0; nseglen=nseg_e-nseg_s;
40             if(nseglen>1)
41                 num_nlen+1 -> num_nlen; MLN = MLN+nseglen;
42     // force the last diagonal line to stop
43     if(seg_new==1)
44         seg_new=0;
45         pseglen=seg_e-seg_s;
46         if(pseglen>1)
47             num_plen+1->num_plen; MLP = MLP+pseglen;
48     if(nseg_new==1)
49         nseg_new=0;
50         nseglen=nseg_e-nseg_s;
51         if(nseglen>1)
52             num_nlen+1 -> num_nlen; MLN = MLN+ nseglen;
53     // end of the l loop
54     MLP =MLP/num_plen;
55     MLN =MLN/num_nlen;
56     CAR1=MLP/MLN;
57     TC =TC/ Totnum_cc;
58     TAC=TAC/ Totnum_cc;
59     CAR2=TC/TAC;

```

Algorithm and implementation

Calculating the entire TCM matrix and then the parameters requires large computer memory and long computation time. Instead, we calculated the TCM properties on the fly. Because the TCM matrix is symmetric, we only considered the upper triangle matrix to save time. The main computation loop is for different delay. In the TCM matrix, each diagonal corresponds to a specific delay between the assessed two embedding vectors. By looping over the diagonals, we managed to calculate the aforementioned TCM matrix properties without pre-calculating the entire matrix. Detailed algorithm for TCM and the property calculation was given in Algorithm 1. “gap” is an integer here for increasing the time interval between adjacent embedding vectors. In fMRI, embedding vectors with a few timepoints away often show very high correlation coefficients due to the hemodynamic response function convolution. As a result, the binarized TCM matrix has many long lines in the diagonals within the nearest neighborhood of the main diagonal. These diagonals may even appear as entire continuous lines and will dominate the calculation of the mean length of the diagonal lines and result in a nearly constant value across different subjects. To avoid their influence, we introduced a parameter DIA_S to exclude the diagonals near the main diagonal from the several TCM parameter calculations. This number has been empirically verified to be between $1/4w$ and $1/2w$. DIA_E is used to exclude the last several diagonals because they are relatively too short to provide sufficient points to find reliable continuous line segments.

The algorithm was implemented in C++ using CUDA (the parallel computing programming platform created by Nvidia Inc). Similar to the brain entropy mapping (Wang, Li et al. 2014, Wang 2021) CUDA acceleration, we used parallelism across within-brain voxels.

Experiments

To evaluate the effects of w and r on temporal coherence characterization, we extracted mean time series from the first rsfMRI scan (the first LR scan) of 20 HCP subjects from the posterior

cingulate cortex (PCC). 20 1/f noise and gaussian noise were also generated. TCM was performed using the above algorithm with different w and r values: w varied from 30 to 90 with a step of 10; r varied from 0.2 to 0.6 with a step of 0.1. TC, TAC, CAR1, MLP, MLN, and CAR2 were calculated. Analysis of variance (ANOVA) and paired-t test were used to statistically infer the effects of w when r was fixed or the effects of r when w was fixed.

We then calculated TC, TAC, CAR1, MLP, MLN, and CAR2 at each voxel for the 862 HCP subjects four rsfMRI data. Four Nvidia GTX 1080 Titan graphic processing unit (GPU) video cards were used to accelerate the process. The collections of each measure at all voxels form a corresponding map, which was called as a temporal coherence map (TCM). For each subject, each of the six TCMs was averaged across the first LR and the first RL rsfMRI scans to minimize the potential effects of the phase encoding polarities. For the simplicity of description, the mean TCMs were called REST1 TCMs. The same averaging process was performed for these parametric maps calculated from the second LR and the second RL rsfMRI scans, and we called the mean TCMs as REST2 TCMs. $w=30, 60, 90$, and $r=0.3$ and 0.5 were used.

Test-retest stability

TCM test-retest stability was assessed by the intra-class correlation (ICC) (Shrout and Fleiss 1979) between the corresponding REST1 and REST2 TCMs, i.e., for each of the six TCMs separately.

Statistical analyses on the biological and cognitive associations of TCMs.

To find the potential biological or neuropsychological associations of resting brain TCM properties, we performed several voxelwise regression analyses for each of the six TCMs collected at the REST1 session (averaged across the first LR and the RL scans) and the REST2 session (averaged across the second LR and the RL scans), separately. Biological measures included

age and sex. Cognitive capability was measured by the total cognitive function composite score (CogTotalComp_Unadj) in the NIH toolbox (<http://www.nihttoolbox.org>) that is derived by averaging the normalized scores of each of the included fluid and crystalized cognition measures and then deriving scale scores based on the new data distributions. Higher scores mean higher levels of cognitive functioning. Sex, age, and education years were included as nuisance variables when the correlation between TCM and the total cognitive scores was examined with multiple regression analysis. The multiple regression model was built and estimated using SPM (<https://www.fil.ion.ucl.ac.uk/spm/>).

The voxelwise significance threshold for assessing each of the association analysis results was defined by $p < 0.05$. Multiple comparison (across voxels) correction was performed with the family wise error theory (Nichols and Hayasaka 2003). Image and statistical results were displayed using Mricron (<https://www.nitrc.org/projects/mricron>) developed by Chris Rorden.

Results

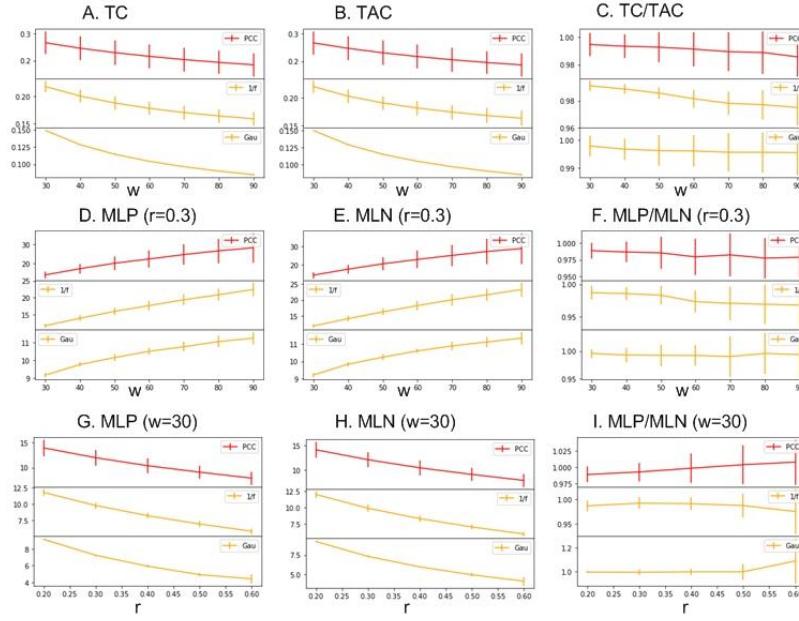


Fig. 3. TCM measures at different embedding vector length (w , the horizontal axis) and r . A, B, C are independent of r . $r=0.3$ in D, E, and F. $w=30$ in G, H, and I. Error bars indicate STD of the measures from 20 different samples of each of the three time series.

Effects of w on TC, TAC, and CAR1

Fig. 3 shows the evaluation results of TCM with different parameters, w , and r , for the three time series. Both ANOVA and paired-t tests were used to assess the effects of different w values on TC, TAC, and CAR1. ANOVA was used to assess the overall effects of w , while paired-t test was used to assess the TCM measure difference between two different w values. For each time series, TC (Fig. 3A) and TAC (Fig. 3B) both decreased with w ($p < 7.6e-8$, one way ANOVA for each of the three time series). The corresponding changes caused by different w were statistically significant with $p < 8.4e-11$ (paired-t test, two tailed for each possible pair of w values). Fig. 3C shows a trend of decreasing CAR1 when w increases but the sensitivity of CAR1 to w was much less than that in TC and TAC. Only 1/f noise showed significantly ($p < 7.7e-10$, one-way ANOVA) decreasing CAR1 when w increases. CAR1 of 1/f noise showed statistically significant changes when w changed from one value to another ($p < 0.016$, two-tailed paired-t test). For the PCC rsfMRI

time series, CAR1 of $w=90$ was significantly different from CAR1 at other w values ($p<0.022$, paired t-test, two tailed).

Effects of w on MLP, MLN, and CAR2

Fig. 3D and 3E show that both MLP and MLN increases with w . Both ANOVA and paired-t test were used to assess the effects of different w values on MLP, MLN, and CAR2. These assessments were made for each r separately. For each assessed r (from 0.2 to 0.6), MLP showed statistically significant ($p<0.024$, one-way ANOVA, the factor is w) increase in all three signals except for Gaussian noise when $r\geq 0.5$. MLN increases with w ($p<0.0003$, one-way ANOVA, the factor is w) for all three signals for all r values except for Gaussian noise when $r\geq 0.4$. CAR2 changes (Fig. 3F) in response to w were only significant in 1/f noise for $r=0.2$, 0.3, and 0.4 and in Gaussian noise for $r=0.4$. MLP differences between any two w values for any of the r value were statistically significant ($p<0.0014$, two tailed paired t-test). MLN differences between any two w values for any assessed r value were statistically significant ($p<0.0016$, two tailed paired t-test). CAR2 of the PCC rsfMRI time series and Gaussian noise did not differ across w for most of r values. CAR2 of 1/f noise showed statistically significant differences in 1/3 of the total number of paired-t test.

Effects of r on MLP, MLN, and CAR2

Fig. 3D and 3E show that both MLP and MLN decrease with r . ANOVA and paired-t test were used to assess the effects of r on MLP, MLN, and CAR2 for each w separately. For each assessed w (from 30 to 90), MLP showed statistically significant ($p<1.7e-12$, one-way ANOVA, the factor is r) decrease in all three signals. MLN decreases with r ($p<1e-12$, one-way ANOVA, the factor is w) for all three signals. CAR2 did not differ across r for both the PCC rsfMRI signal and 1/f noise. CAR2 of Gaussian noise significantly differed across r when $w=30$ ($p=0.0054$,

one-way ANOVA). MLP was significantly different between two different r values in all three signals for all w values ($p < 8.9e-5$, two tailed paired t-test) except in Gaussian noise and when $w=90$. MLN was significantly different between two different r values in all three signals for all w values ($p < 0.0024$, two tailed paired t-test). CAR2 was not significantly different between two different r values in all three signals for most of w values.

Effects of w on the cross-signal TC, TAC, and CAR1 difference

TC, TAC, and CAR1 significantly differed across the three signals at all assessed w ($p < 0.04$ for all possible two-sample t-test on each of the three property measures for any two of the three signals).

Effects of w and r on the cross-signal MLP, MLN, and CAR2 difference

MLP, MLN, and CAR2 can significantly differentiate the three signals for all assessed w and r ($p < 0.043$ for all possible two-sample t-test on each of the three property measures for any two of the three signals).

Mean TCMs

TCMs calculated with different w and r were very similar though the intensity was different. Both ICC and the correlation analyses showed very similar results for different w and r too. Based on the synthetic data and the result similarity of the in vivo data, we only showed results based on $w=30$ and $r=0.3$ below.

Fig. 4 shows the mean TCMs of REST1 (the first LR and RL rsfMRI scans) of all 862 subjects. TC, TAC, MLP, and MLN had very similar image contrast with high value in the cortical region

and lower value in subcortical area and white matter (note that most part of white matter has been masked out during TCM calculations in order to save computation time). Similar to results of the synthetic data, MLP and MLN are shorter than 15, i.e., w/2. CAR1 (Fig. 4C) and CAR2 (Fig. 4F) showed very different contrast. CAR1 was smaller than 1 in the entire brain. Image contrast of CAR1 looks opposite to that of TC, TAC, MLP, or MLN. Cortical CAR1 was smaller than white matter and subcortical CAR1. CAR2 in white matter and subcortical regions was almost 0. CAR2 in many cortical areas was ≤ 1 , but was >1 in visual cortex, motor cortex, and part of prefrontal cortex.

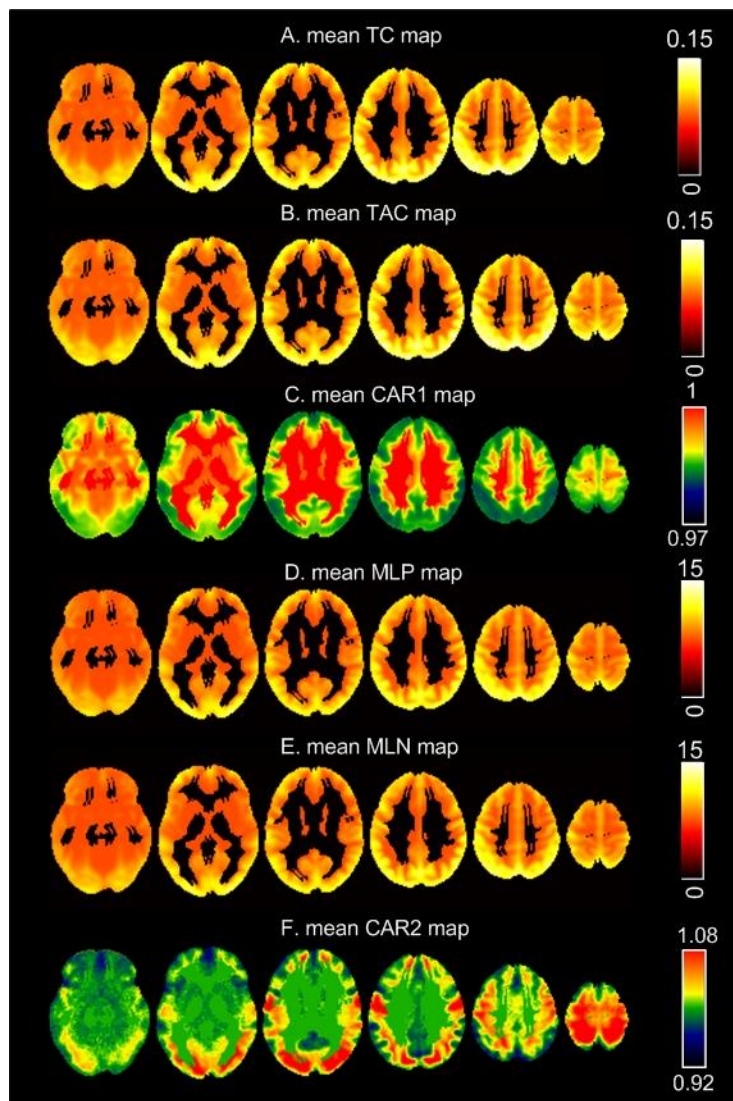


Fig. 4. Mean TCMs of all subjects at the REST1 session. Display window for each map was determined by the colorbar on the right.

Test-retest analysis results

Fig. 5 shows the ICC maps thresholded at $ICC \geq 0.3$. TC, TAC, MLP, and MLN showed high ICC in the entire brain (note that most part of white matter was masked out during TCM calculation). CAR1 and CAR2 were much less reliable. CAR1 showed moderate ICC values in cingulate cortex, insula, primary visual cortex, orbitofrontal cortex, dorsolateral prefrontal cortex, and inferior temporal lobe. CAR2 was non-stable in nearly the entire brain except a small part motor cortex and visual cortex.

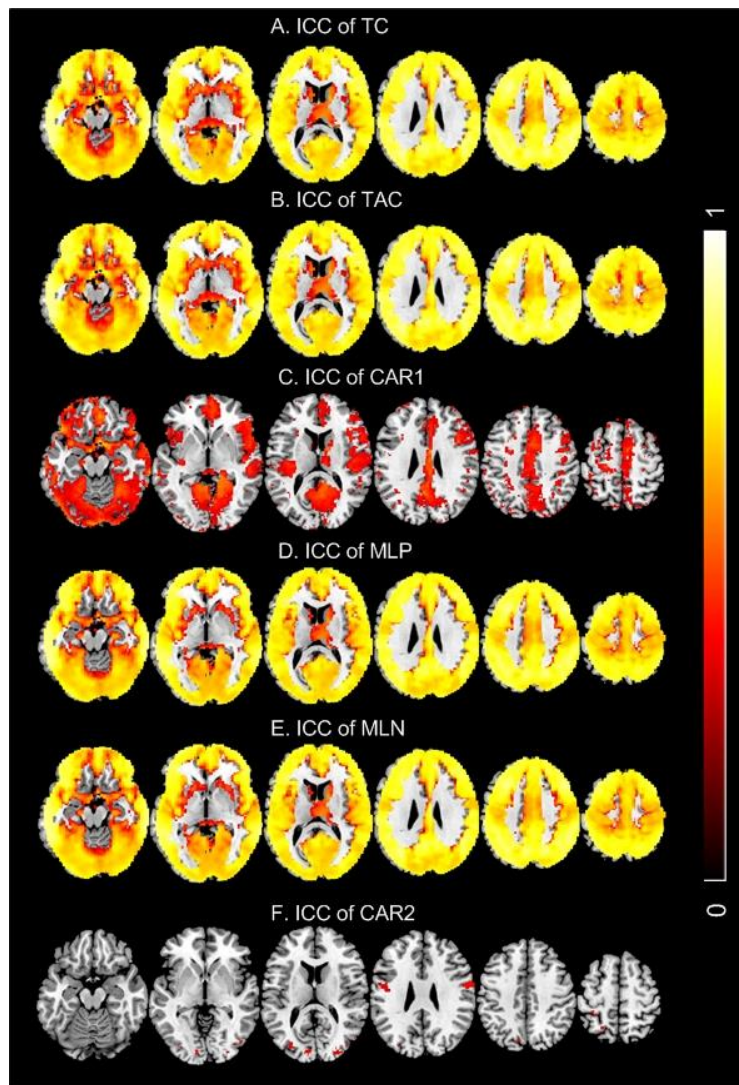


Fig. 5. ICC maps of the six TCMs: A) TC, B) TAC, C) CAR1, D) MLP, E) MLN, F) CAR2. ICC maps were overlaid on top of the MNI standard brain. The cutoff used to threshold the ICC maps was 0.3. The colorbar indicates the display window of the ICC values.

Biological and cognitive associations of TCMs

Fig. 6 shows the voxelwise correlations between each of the six TCMs and age. TC/TAC/MLP/MLN all showed significant ($p < 0.05$, multiple comparison corrected using the family-wise error (FWE) based method, corresponding to $Z = 5.15$) correlations to age in prefrontal cortex,

parietal cortex, and temporal lobe. CAR1 (Fig. 6C) was positively ($p < 0.05$, FWE corrected) correlated with age in temporal cortex, insula, right lateral prefrontal cortex, and lateral parietal cortex. CAR2 (Fig. 6F) was positively correlated with age ($p < 0.05$, FWE corrected) in middle prefrontal cortex, anterior cingulate cortex, insula, and a small part of parietal cortex.

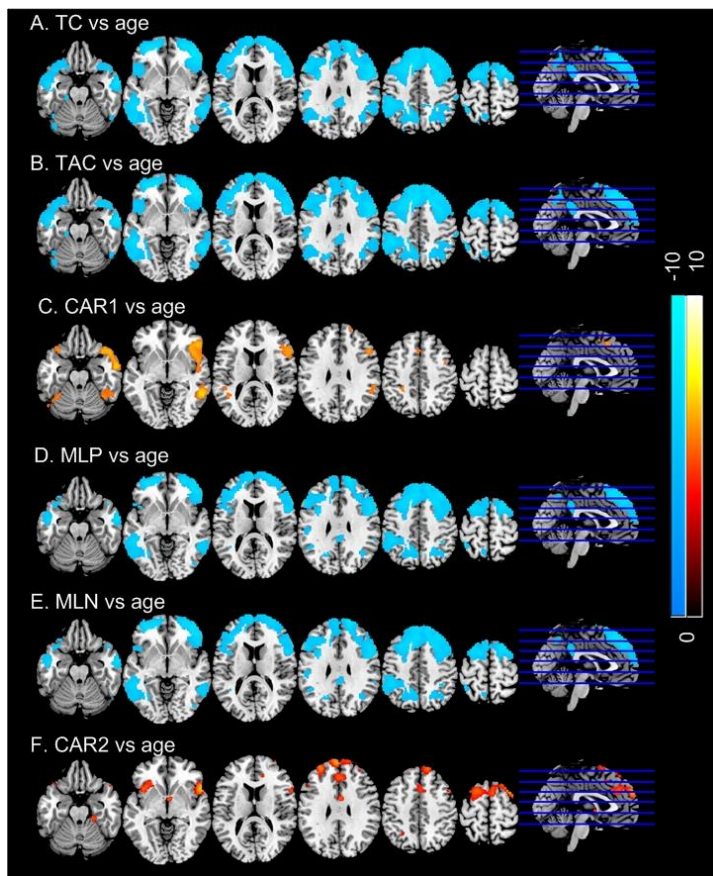


Fig. 6. Correlations of regional TCMs with age: A) TC, B) TAC, C) CAR1, D) MLP, E) MLN, F) CAR2. Significance level was defined by $p < 0.05$ (FWE corrected). Blue means negative correlation; hot color means positive correlations. Colorbars indicate the display window of the Z-scores of the age vs TCM regressions.

Fig. 7 shows the sex effects on TCMs. Female had lower ($p < 0.05$, FWE corrected) TC/TAC/MLP/MLN than male in temporal cortex, insula, parietal cortex, motor cortex, part of prefrontal cortex, and visual cortex. CAR1 (Fig. 7C) was higher in female in temporal cortex, the entire cingulate cortex, the entire visual cortex, the entire parietal cortex, and a large portion of prefrontal cortex. Sex effects on CAR2 (Fig. 7F) were more focused on the posterior part of the brain including visual cortex, posterior temporal cortex, and parietal cortex in addition to a small portion of prefrontal cortex.

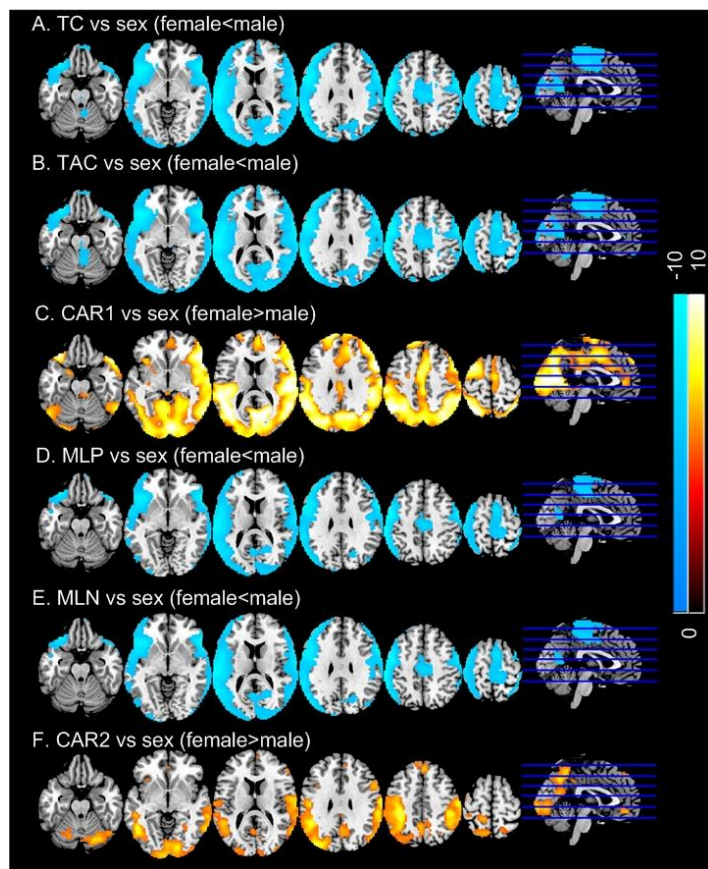


Fig. 7. Sex effects on regional TCMs: A) TC, B) TAC, C) CAR1, D) MLP, E) MLN, F) CAR2. Significance level was defined by $p < 0.05$ (FWE corrected). Blue means female lower than male; hot color means higher in female. Colorbars indicate the display window of the Z-scores of female vs male TCM two-sample t-test.

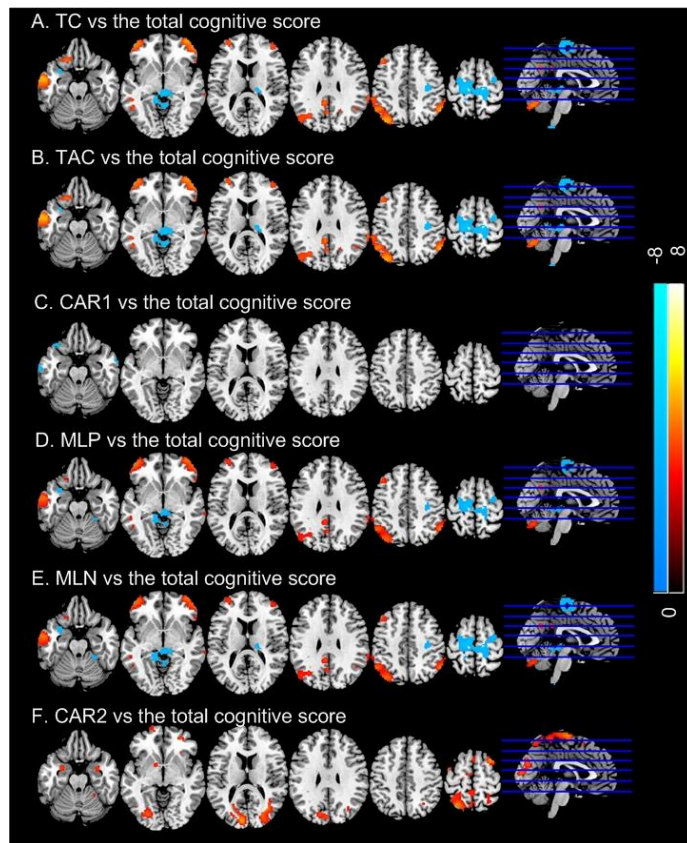


Fig. 8. Cognitive correlations of TCMs: A) TC, B) TAC, C) CAR1, D) MLP, E) MLN, F) CAR2. Significance level was defined by $p < 0.05$ (FDR corrected). Blue and hot color indicate negative and positive correlation, respectively. Colorbars indicate the display window of the Z-scores of regression analysis.

Fig. 8 shows the correlations of TCMs with the total cognitive score. TC/TAC/MLP/MLN showed quite similar cognitive correlation patterns (Fig. 8A, 8B, 8D, 8E, $p < 0.05$, multiple comparison correction was done with the false discovery rate (FDR) method). The four measures were positively correlated with total cognitive score in temporal cortex, lateral prefrontal cortex, parietal cortex, and cerebellum. They were negatively correlated with cognitive score in motor cortex and thalamus. CAR1 (Fig. 8C) only showed negative correlations with the cognitive score in temporal

cortex while CAR2 (Fig. 8F) only showed positive correlations with the cognitive score in motor cortex, visual cortex, amygdala, prefrontal cortex, and parietal cortex.

Discussion

We presented a method to exam temporal coherence, temporal incoherence, and their ratio in a given time series measured from a dynamic system. The method was dubbed as TCM (temporal coherence mapping) and was based on the correlation coefficient matrix of the temporal embedding vectors. These vectors were extracted to expand the one-dimensional time series to a multiple dimension domain so that the cross-transit state information collapsed in the original one-dimensional space can be better studied. We assessed six typical properties of the temporal coherence matrix. Both synthetic data and in-vivo rsfMRI data were used to evaluate their stability and potential value for neuroscientific research.

Synthetic data were used to evaluate the effects of the length of the embedding window w and the correlation coefficient threshold r on these parameters. TC, TAC, and CAR1 are independent of r . Longer w reduces TC and TAC because longer embedding vectors introduce more variance and subsequently reduces correlation coefficients. CAR1, the ratio of TC and TAC showed much less sensitivity to w , compared to TC and TAC alone. This is because that the changes of TC and TAC due to the change of w were cancelled out during the division. Both MLP and MLN were shorter than half of the window length. Half of the window can be approximately treated as half of the cycle for the signal observed in the window. Shifting half cycle of a periodic signal will flip the sign of the correlation of two embedding vectors. For non-periodic signal, this change will occur faster and result in a shorter-than half window length MLP or MLN. Gaussian signal has a wider spectrum than others and the correlation cancellation due to the number of changed embedding vector elements is faster, which explains the result that Gaussian signal has the shortest MLP and MLN. The above description about the dependence of MLP and MLN on the window length

also explains why MLP and MLN both nonlinearly increase with w . We should note that this dependence is linked with the Pearson correlation. It may not exist if we changed to other measures to calculate the similarity between a pair of vectors (such as Chebychev distance or L2 distance). Changing w did not change CAR2 for most of assessed cases because of the division-induced cancelation. MLP and MLN both decreases with r . This is because thresholding the correlation matrix with larger r will reduce the number of suprathreshold vector pairs in general. Again, this decreasing trend was cancelled out in CAR2 due to the division. When the same w and r were used, the six parameters can differentiate the three assessed signals, suggesting that w and r have negligible effect on TCM measures for differentiating signals with known temporal coherence difference if the same values are used in TCM calculations.

When applied to 862 young healthy subjects' rsfMRI data, we collected the whole brain maps of the six TCM property measures. The maps of TC, TAC, MLP, and MLN had very similar image contrast with high value in the cortical region and lower value in subcortical area and white matter. These findings are consistent with our recent work in brain entropy mapping using rsfMRI from HCP(Wang 2021). In grey matter, the highest temporal coherence located in the prefrontal and parietal area which are well known to have predominant slowly fluctuating resting state activity(Raichle, MacLeod et al. 2001, Fransson 2005, Buckner and Vincent 2007, Raichle and Snyder 2007). The high resemblance between TC and TAC maps suggests a tight coupling between coherence and anti-coherence. The high resemblance between MLP and MLN maps suggests that brain regions with coherent transit states staying in parallel have anti-correlated transit states staying for a similar duration of time. The high similarity between TC maps and MLP maps suggests that brain regions that showed higher coherence also had transit states staying parallel for longer time. The high similarity between TAC maps and MLN maps suggests that brain regions that showed higher anti-coherence also had anti-correlated transit states staying anti-correlated for longer time. CAR1 and CAR2 showed very different contrast than the other four

TCMs. Image contrast of CAR1 looks opposite to that of TC, TAC, MLP, or MLN, with the lowest CAR1 value in the prefrontal and parietal area. CAR1 was smaller than one, indicating that resting brain activity measured by rsfMRI contains more anti-correlated transit states. CAR1 in grey matter was smaller than white matter and subcortical regions, suggesting a larger imbalance of coherence and anti-coherence in the cortical regions. While this study represents the first effort to characterize coherence and anti-coherence separately in fMRI, the similar distribution patterns of TC and TAC, MLP and MLN, and the patterns of CAR1 and CAR2 suggest a stable balance between the macroscopic brain coherence and anti-coherence, which might represent way to coordinate brain excitation and inhibition across large time scale.

TC, TAC, MLP, and MLN showed very high test-retest stability in the entire cerebral cortex, subcortical region, and cerebellum. CAR1 and CAR2 were much less reliable. CAR1 showed moderate ICC values in cingulate cortex, insula, primary visual cortex, orbitofrontal cortex, dorsolateral prefrontal cortex, and inferior temporal lobe. CAR2 was non-stable in nearly the entire brain except a small part motor cortex and visual cortex. The much lower stability of CAR1 and CAR2 was partly caused by noise amplification during the division process. Low stability of CAR1 and CAR2 also indicates that changes of the balance is dynamic in the healthy brain.

Coherence and anti-coherence maps showed significant age effects in temporal cortex, prefrontal cortex, and parietal cortex. TC, TAC, MLP and MLN all decrease with age. However, CAR1 and CAR2 only showed positive correlations with age in temporal pole, insula, and prefrontal cortex, suggesting an age-related imbalanced decrease of anti-coherent activity as compared to coherent activity decrease. Females showed significantly lower coherence and anti-coherence activity than males as reflected by the lower TC, TAC, MLP, and MLN in females. Both CAR1 and CAR2 showed that the sex effects on the anticoherent activity (measured by TAC and MLN) are stronger than the coherence activity, which results in higher CAR1 and CAR2 in females than in males.

Lower coherent and anti-coherent activity in females was consistent with the higher entropy findings previously reported (Li, Fang et al. 2016, Wang 2021).

LRTCs have been demonstrated to be crucial to high-order brain functions (Pesaran, Pezaris et al. 2002, Buzsáki and Draguhn 2004, Womelsdorf, Fries et al. 2006, Womelsdorf, Fries et al. 2006, Buschman and Miller 2007, Saleh, Reimer et al. 2010, Dean, Hagan et al. 2012, Thut, Miniussi et al. 2012, Palva, Zhigalov et al. 2013, Botcharova, Farmer et al. 2014, Wong, Fabiszak et al. 2016, Shewcraft, Dean et al. 2020). Our TCM vs total cognitive score correlations are consistent with the literature. Very similar cognitive associations were found in the coherence TCMs and the anti-coherence TCMs, suggesting that coherence and anti-coherence are equally important for brain cognition. The four coherence and incoherence measures were positively correlated with total cognitive score in temporal cortex, lateral prefrontal cortex, parietal cortex, and cerebellum. Negative correlations were found in the motor system. These regions are well known to have large slowly fluctuating resting state activity (Biswal, Yetkin et al. 1995, Greicius, Srivastava et al. 2004, Biswal, Mennes et al. 2010, Damoiseaux, Prater et al. 2012). Our recent study (Wang 2021) has suggested that lower entropy in those regions may indicate a larger capacity of brain function reserve as supported by the negative correlations between entropy and general intelligence and general functionality and the existing speculations that resting state brain activity in these regions may play a role in maintaining and facilitating brain functions (Raichle, MacLeod et al. 2001, Raichle and Gusnard 2002, Raichle 2006). Since entropy indirectly reflects coherence, our findings of the positive TCM vs total cognitive score correlations in the frontal, parietal, and cerebellum are consistent with that study (Wang 2021). Coherent motor system resting activity has been well characterized using functional connectivity analysis (Biswal, Yetkin et al. 1995). In this study, we found that lower coherence and anti-coherence in motor cortex was associated with better cognitive capability. The associations of TCMs in motor system can be explained by the intense interactions between motor and cognitive functions for cognitive

functions often need involvement of motor function (Leisman, Moustafa et al. 2016). Since less coherent activity indicates a larger number of transit states, the negative motor system TCM vs cognitive function correlations may then suggest that more transit states are required to support a better cognitive capability.

Conclusion

Temporal embedding based TCM provides a potentially useful tool to assess brain coherence and anti-coherence and their balance. The coherence/anticohherence measures are stable across repeated measurement. They are correlated with biological and psychological measures, making them potentially valuable metrics for cognitive or translational research.

Reference

- Beggs, J. M. and D. Plenz (2003). "Neuronal avalanches in neocortical circuits." Journal of neuroscience **23**(35): 11167-11177.
- Biswal, B., F. Z. Yetkin, V. M. Haughton and J. S. Hyde (1995). "Functional Connectivity in the Motor Cortex of Resting Human Brain Using Echo-Planar Mri." Magnetic Resonance in Medicine **34**(4): 537-541.
- Biswal, B. B., M. Mennes, X. N. Zuo, S. Gohel, C. Kelly, S. M. Smith, C. F. Beckmann, J. S. Adelstein, R. L. Buckner, S. Colcombe, A. M. Dogonowski, M. Ernst, D. Fair, M. Hampson, M. J. Hoptman, J. S. Hyde, V. J. Kiviniemi, R. Kotter, S. J. Li, C. P. Lin, M. J. Lowe, C. Mackay, D. J. Madden, K. H. Madsen, D. S. Margulies, H. S. Mayberg, K. McMahon, C. S. Monk, S. H. Mostofsky, B. J. Nagel, J. J. Pekar, S. J. Peltier, S. E. Petersen, V. Riedl, S. A. Rombouts, B. Rypma, B. L. Schlaggar, S. Schmidt, R. D. Seidler, G. J. Siegle, C. Sorg, G. J. Teng, J. Veijola, A. Villringer, M. Walter, L. Wang, X. C. Weng, S. Whitfield-Gabrieli, P. Williamson, C. Windischberger, Y. F. Zang, H. Y. Zhang, F. X. Castellanos and M. P. Milham (2010). "Toward discovery science of human brain function." Proceedings of the National Academy of Sciences of the United States of America **107**(10): 4734-4739.
- Botcharova, M., S. F. Farmer and L. Berthouze (2014). "Markers of criticality in phase synchronization." Frontiers in systems neuroscience **8**: 176.
- Buckner, R. L. and J. L. Vincent (2007). "Unrest at rest: default activity and spontaneous network correlations." Neuroimage **37**(4): 1091-1096.
- Buschman, T. J. and E. K. Miller (2007). "Top-down versus bottom-up control of attention in the prefrontal and posterior parietal cortices." science **315**(5820): 1860-1862.
- Buzsáki, G. and A. Draguhn (2004). "Neuronal oscillations in cortical networks." science **304**(5679): 1926-1929.
- Da Chang, D. S., Jian Zhang, Yuanqi Shang, Qiu Ge, Ze Wang (2018). "Caffeine caused a widespread increase of resting brain entropy." Scientific Reports **8**: 2700.
- Damoiseaux, J. S., K. E. Prater, B. L. Miller and M. D. Greicius (2012). "Functional connectivity tracks clinical deterioration in Alzheimer's disease." Neurobiol Aging **33**(4): 828 e819-830.

Dean, H. L., M. A. Hagan and B. Pesaran (2012). "Only coherent spiking in posterior parietal cortex coordinates looking and reaching." Neuron **73**(4): 829-841.

Deco, G. and V. K. Jirsa (2012). "Ongoing Cortical Activity at Rest: Criticality, Multistability, and Ghost Attractors." Journal of Neuroscience **32**(10): 3366-3375.

Donghui Song, D. C., Jian Zhang, Qiu Ge, Yu-Feng Zang, Ze Wang (2019). "Associations of Brain Entropy (BEN) to Cerebral Blood Flow and fractional Amplitude of Low-Frequency Fluctuations in the Resting Brain." Brain imaging and behavior **13**(5): 486-1495.

Fransson, P. (2005). "Spontaneous low-frequency BOLD signal fluctuations: an fMRI investigation of the resting-state default mode of brain function hypothesis." Hum Brain Mapp **26**(1): 15-29.

Friedman, N., S. Ito, B. A. Brinkman, M. Shimono, R. L. DeVille, K. A. Dahmen, J. M. Beggs and T. C. Butler (2012). "Universal critical dynamics in high resolution neuronal avalanche data." Physical review letters **108**(20): 208102.

Fries, P. (2005). "A mechanism for cognitive dynamics: neuronal communication through neuronal coherence." Trends in cognitive sciences **9**(10): 474-480.

Fries, P. (2015). "Rhythms for cognition: communication through coherence." Neuron **88**(1): 220-235.

Greicius, M. D., G. Srivastava, A. L. Reiss and V. Menon (2004). "Default-mode network activity distinguishes Alzheimer's disease from healthy aging: evidence from functional MRI." Proc Natl Acad Sci U S A **101**(13): 4637-4642.

Haken, H. (2012). Advanced synergetics: Instability hierarchies of self-organizing systems and devices, Springer Science & Business Media.

He, B. J. (2011). "Scale-free properties of the functional magnetic resonance imaging signal during rest and task." J Neurosci **31**(39): 13786-13795.

He, B. J., J. M. Zempel, A. Z. Snyder and M. E. Raichle (2010). "The temporal structures and functional significance of scale-free brain activity." Neuron **66**(3): 353-369.

Hurst, H. E. (1951). "Long-term storage capacity of reservoirs." Transactions of the American society of civil engineers **116**(1): 770-799.

Leisman, G., A. A. Moustafa and T. Shafir (2016). "Thinking, walking, talking: integratory motor and cognitive brain function." Frontiers in public health **4**: 94.

Li, Z., Z. Fang, N. Hager, H. Rao and Z. Wang (2016). "Hyper-resting brain entropy within chronic smokers and its moderation by Sex." Sci Rep **6**: 29435.

Liu, X., D. Song, Y. Yin, C. Xie, H. Zhang, H. Zhang, Z. Zhang, Z. Wang and Y. Yuan (2020). "Altered Brain Entropy as a predictor of antidepressant response in major depressive disorder." Journal of Affective Disorders **260**: 716-721.

Lu, K., Y. Xu, P. Yin, A. J. Oxenham, J. B. Fritz and S. A. Shamma (2017). "Temporal coherence structure rapidly shapes neuronal interactions." Nat Commun **8**: 13900.

Marwan, N., M. C. Romano, M. Thiel and J. Kurths (2007). "Recurrence plots for the analysis of complex systems." Physics reports **438**(5-6): 237-329.

Moeller, S., E. Yacoub, C. A. Olman, E. Auerbach, J. Strupp, N. Harel and K. Ugurbil (2010). "Multiband multislice GE-EPI at 7 tesla, with 16-fold acceleration using partial parallel imaging with application to high spatial and temporal whole-brain fMRI." Magn Reson Med **63**(5): 1144-1153.

Munoz, M. A. (2018). "Colloquium: Criticality and dynamical scaling in living systems." Reviews of Modern Physics **90**(3): 031001.

Nichols, T. E. and S. Hayasaka (2003). "Controlling the Familywise Error Rate in Functional Neuroimaging: A Comparative Review." Statistical Methods in Medical Research **12**: 419-446.

Nolte, D. D. (2010). "The tangled tale of phase space." Physics today **63**(4): 33-38.

Okun, M. and I. Lampl (2008). "Instantaneous correlation of excitation and inhibition during ongoing and sensory-evoked activities." Nature neuroscience **11**(5): 535-537.

Palva, J. M., A. Zhigalov, J. Hirvonen, O. Korhonen, K. Linkenkaer-Hansen and S. Palva (2013). "Neuronal long-range temporal correlations and avalanche dynamics are correlated with behavioral scaling laws." Proceedings of the National Academy of Sciences **110**(9): 3585-3590.

Peng, C. K., S. Havlin, H. E. Stanley and A. L. Goldberger (1995). "Quantification of scaling exponents and crossover phenomena in nonstationary heartbeat time series." Chaos: an interdisciplinary journal of nonlinear science **5**(1): 82-87.

Pesaran, B., J. S. Pezaris, M. Sahani, P. P. Mitra and R. A. Andersen (2002). "Temporal structure in neuronal activity during working memory in macaque parietal cortex." Nature neuroscience **5**(8): 805-811.

Pesaran, B., M. Vinck, G. T. Einevoll, A. Sirota, P. Fries, M. Siegel, W. Truccolo, C. E. Schroeder and R. Srinivasan (2018). "Investigating large-scale brain dynamics using field potential recordings: analysis and interpretation." Nature neuroscience **21**(7): 903-919.

Raichle, M. E. (2006). "Neuroscience. The brain's dark energy." Science **314**(5803): 1249-1250.

Raichle, M. E. and D. A. Gusnard (2002). "Appraising the brain's energy budget." Proceedings of the National Academy of Sciences of the United States of America **99**(16): 10237-10239.

Raichle, M. E., A. M. MacLeod, A. Z. Snyder, W. J. Powers, D. A. Gusnard and G. L. Shulman (2001). "A default mode of brain function." PNAS **98**: 676-682.

Raichle, M. E. and A. Z. Snyder (2007). "A default mode of brain function: a brief history of an evolving idea." Neuroimage **37**(4): 1083-1090.

Richman, J. S. and J. R. Moorman (2000). "Physiological time-series analysis using approximate entropy and sample entropy." American journal of physiology. Heart and circulatory physiology **278**(6): H2039-2049.

Rubinov, M., O. Sporns, J. P. Thivierge and M. Breakspear (2011). "Neurobiologically Realistic Determinants of Self-Organized Criticality in Networks of Spiking Neurons." Plos Computational Biology **7**(6).

Saleh, M., J. Reimer, R. Penn, C. L. Ojakangas and N. G. Hatsopoulos (2010). "Fast and slow oscillations in human primary motor cortex predict oncoming behaviorally relevant cues." Neuron **65**(4): 461-471.

Shewcraft, R. A., H. L. Dean, M. M. Fabiszak, M. A. Hagan, Y. T. Wong and B. Pesaran (2020). "Excitatory/inhibitory responses shape coherent neuronal dynamics driven by optogenetic stimulation in the primate brain." Journal of Neuroscience **40**(10): 2056-2068.

Shrout, P. E. and J. L. Fleiss (1979). "Intraclass correlations: uses in assessing rater reliability." Psychol Bull **86**(2): 420-428.

Singer, W. (2009). "The Brain, a Complex Self-organizing System." European Review **17**(2): 321-329.

Suckling, J., A. M. Wink, F. A. Bernard, A. Barnes and E. Bullmore (2008). "Endogenous multifractal brain dynamics are modulated by age, cholinergic blockade and cognitive performance." Journal of neuroscience methods **174**(2): 292-300.

Takens, F. (1981). Detecting strange attractors in turbulence. Dynamical systems and turbulence, Warwick 1980, Springer: 366-381.

Teki, S., M. Chait, S. Kumar, S. Shamma and T. D. Griffiths (2013). "Segregation of complex acoustic scenes based on temporal coherence." Elife **2**: e00699.

Thut, G., C. Miniussi and J. Gross (2012). "The functional importance of rhythmic activity in the brain." Current Biology **22**(16): R658-R663.

Wang, Z. (2020). "Assessing the neurocognitive correlates of resting brain entropy." arXiv preprint arXiv:2004.13256.

Wang, Z. (2021). "The neurocognitive correlates of brain entropy estimated by resting state fMRI." NeuroImage in press.

Wang, Z. and A. s. D. N. Initiative (2020). "Brain Entropy Mapping in Healthy Aging and Alzheimer's Disease." Frontiers in Aging Neuroscience **12**.

Wang, Z., Y. Li, A. R. Childress and J. A. Detre (2014). "Brain Entropy Mapping Using fMRI." PLoS One **9**(3): e89948.

Willshaw, D. (2006). "Self-organization in the nervous system." Cognitive systems: Information processing meet brain science: 5-33.

Wink, A. M., E. Bullmore, A. Barnes, F. Bernard and J. Suckling (2008). "Monofractal and multifractal dynamics of low frequency endogenous brain oscillations in functional MRI." Human brain mapping **29**(7): 791-801.

Womelsdorf, T., P. Fries, P. P. Mitra and R. Desimone (2006). "Gamma-band synchronization in visual cortex predicts speed of change detection." Nature **439**(7077): 733-736.

Womelsdorf, T., P. Fries, P. P. Mitra and R. Desimone (2006). "Gamma-band synchronization in visual cortex predicts speed of change detection." Nature **439**(7077): 733.

Wong, Y. T., M. M. Fabiszak, Y. Novikov, N. D. Daw and B. Pesaran (2016). "Coherent neuronal ensembles are rapidly recruited when making a look-reach decision." Nature neuroscience **19**(2): 327-334.

Xue, S. W., Q. Yu, Y. Guo, D. Song and Z. Wang (2019). "Resting-state brain entropy in schizophrenia." Compr Psychiatry **89**: 16-21.

Zhou, F., Y. Zhuang, H. Gong, J. Zhan, M. Grossman and Z. Wang (2016). "Resting State Brain Entropy Alterations in Relapsing Remitting Multiple Sclerosis." PLoS One **11**(1): e0146080.